Transmission Microscopy with Nanometer Resolution Using a Deterministic Single Ion Source

Georg Jacob,[1,*] Karin Groot-Berning,[1] Sebastian Wolf,[1] Stefan Ulm,[1] Luc Couturier,[1,†] Samuel T. Dawkins,[1] Ulrich G. Poschinger,[1] Ferdinand Schmidt-Kaler,[1] and Kilian Singer[2,1]

[1]*QUANTUM, Institut für Physik, Universität Mainz, Staudingerweg 7, 55128 Mainz, Germany*

[2]*Institut für Physik, Universität Kassel, Heinrich-Plett-Straße 40, 34132 Kassel, Germany*

(Received 3 December 2015; published 20 July 2016)

We realize a single particle microscope by using deterministically extracted laser-cooled $^{40}Ca^{+}$ ions from a Paul trap as probe particles for transmission imaging. We demonstrate focusing of the ions to a spot size of 5.8 ± 1.0 nm and a minimum two-sample deviation of the beam position of 1.5 nm in the focal plane. The deterministic source, even when used in combination with an imperfect detector, gives rise to a fivefold increase in the signal-to-noise ratio as compared with conventional Poissonian sources. Gating of the detector signal by the extraction event suppresses dark counts by 6 orders of magnitude. We implement a Bayes experimental design approach to microscopy in order to maximize the gain in spatial information. We demonstrate this method by determining the position of a 1 μm circular hole structure to a precision of 2.7 nm using only 579 probe particles.

DOI: 10.1103/PhysRevLett.117.043001

The advancement of electron microscopes [1,2] and subsequently ion microscopes [3–5] has often been driven by new or improved types of sources. Together with improvements to imaging optics, better sources have helped to push the resolution of imaging far below the diffraction limit of visible light [6,7], enabling substantial progress across various scientific [8] and industrial [9] fields. More recently, techniques pioneered in cold atoms have been employed to improve the sources in terms of phase space occupation [10,11], temporal control [12,13], and offering deterministic emission properties [14,15]. In this Letter, we implement a single ion source by extracting laser-cooled $^{40}Ca^{+}$ ions from a linear segmented Paul trap [16,17] and use it to realize a novel type of microscopy based on deterministic probing.

In conventional microscopy, the signal-to-noise ratio (SNR) can typically be improved by increasing the exposure time or flux. This is a direct consequence of the Poissonian statistics of the sources in use. However, a high particle emission can be detrimental in some applications where, for example, high irradiation causes charging [18], contamination, or even damage [19] to samples. The approach presented here addresses this problem in a fundamentally different way, namely, by probing with a deterministic source. In principle, such a source could give rise to noiseless imaging, requiring an exposure of only a single particle to probe for transmission. However, in combination with a detector of finite quantum efficiency, the signal statistics become binomial. This still leads to inherently more information per particle and, thus, higher SNRs than would be possible with Poissonian statistics. In addition, the source permits gating of the detection by the extraction event, yielding a suppression of the detector dark counts by 6 orders of magnitude. Finally, with a deterministic source, the Bayes experimental design method can be used to maximize the spatial information gained when imaging transmissive structures with a parametrizable transmission function.

Setup.—The experiment is based on a Paul trap which is constructed from four microfabricated alumina chips arranged in an X-shaped configuration and two metal end caps [see Fig. 1(a)]. Each chip comprises 11 electrodes for shaping the confining electrostatic potential along the axial direction. We operate the device at trap frequencies $\omega/(2\pi)$ of 0.58 to 0.85 MHz and 1.4 to 3.3 MHz for the axial and radial modes of vibration, respectively.

The deterministic source is implemented by a fully automated procedure: Initially, a random number of calcium ions are loaded by photoionization and laser cooled on the $S_{1/2}$ to $P_{1/2}$ dipole transition near 397 nm. The number of ions is counted by imaging the ion fluorescence on a CCD camera and then reduced to the desired number by lowering the axial trapping potential with a predefined voltage sequence, which is applied to the trap segments [Fig. 1(a)]. The cold ions are extracted along the axial direction of the trap by application of an acceleration voltage of up to -6 kV to one of the pierced end caps (-5.9 kV for experiments reported here). Fast high voltage solid-state switches limit the jitter to less than 1 ns. The extraction time is synchronized to the phase of the radio-frequency trap drive [$\Omega/(2\pi) = 23$ MHz] with adjustable delay. With this method, we attain rates for loading and extraction of single ions of up to 3 s^{-1}. Ions leave the trap passing through the 200 μm diameter hole in the end cap and are detected by a secondary electron multiplier with a quantum efficiency of about 96%.

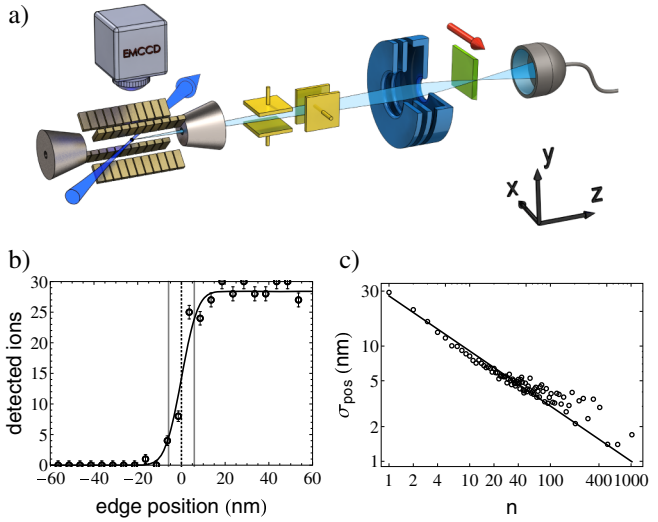

FIG. 1. (a) Sketch of the single ion microscope. (b) Number of detected ions out of 30 single ion extractions at the corresponding profiling edge position (circles). Errors are determined from binomial counting statistics. Dashed line shows center position and gray lines show 1σ radius of the beam waist. Fitting a Gaussian error function $p(x) = (a/2)[1 + \mathrm{erf}((x - x_0)/\sigma\sqrt{2})]$ to the data yields $a = 28.1 \pm 0.5$ and $\sigma = 5.8 \pm 1.0$ nm. (c) Log-log plot of the two-sample deviation of the beam position σ_{pos} versus the number of consecutive profiling edge measurements n. The fit (black line) to the beam position deviations (circles) reveals a slope of -0.48 ± 0.01. Integration time for $n = 10$ is about 5 min; for $n = 100$ it is about 1 h.

We measure a time-of-flight signal with a half-width half-maximum spread of $\Delta t = 270$ ps. This corresponds to a velocity spread of $\Delta v = 8$ m/s at a typical average speed of 10^5 m/s.

In order to align and scan the beam [Fig. 1(a), light blue], deflection electrodes are placed along the extraction path [Fig. 1(a), yellow]. For focusing of the beam, an electrostatic einzel lens with an open aperture of 4 mm is used [Fig. 1(a), blue]. The lens' geometry parameters are optimized by electrostatic simulations [20] to minimize spherical aberration. Chromatic aberration is strongly suppressed due to the narrow velocity distribution of the ions. Image information is generated by recording transmission events for a well-defined number of extractions while scanning the position of an object [Fig. 1(a), green] in the focal plane using a three-axis translation stage.

Beam waist and beam stability.—The spatial resolution of the beam in the focal plane is determined by stepping a profiling edge into the beam and performing a fixed number of transmission measurements at each position. Under optimal operating conditions, we measure 5.8 ± 1.0 nm for the 1σ radius of the focus [Fig. 1(b)]. We conjecture this resolution is limited by mechanical vibrations, since contributions due to spherical aberration, chromatic aberration, and electrical noise are estimated to be orders of magnitude lower. Reducing these vibrations and cooling to the ground state would lead to a spot size of 0.5 nm, assuming a wave packet size of about 15 nm and the current magnification factor of 28. This would be around an order of magnitude above the resolution of state-of-the-art transmission electron microscopy [21]. Effects due to surface charging were never observed, even when using a nonconducting profiling edge. Indeed, using a simple deflection model, we estimate the number of surface charges per pixel needed to degrade a resolution of 1 nm to be approximately 10^3, which is well above the maximum attainable charge density estimated from the breakdown field strength.

The long-term stability of the system is validated by evaluating the two-sample deviation of the lateral position of the focus [see Fig. 1(c)]. To this end, 2048 profiling edge measurements [similar to those in Fig. 1(b)] were carried out, repetitively. Every measurement comprises 26 contiguous profiling edge positions separated by 10 nm, each probed with a single ion. In total, the data set contains 53 248 extraction events within an acquisition time of 18 h. The two-sample variance [see Fig. 1(c)] is given by

$$\sigma^2_{\mathrm{pos}}(n) = \frac{1}{2(N-1)} \sum_{i=0}^{N-1} (\bar{x}_{i+1}(n) - \bar{x}_i(n))^2,$$

where $\bar{x}_i(n)$ is the beam position for the ith segment derived from fitting to the aggregate count data from n consecutive profiling edge measurements.

If the measurements are dominated by statistical fluctuations rather than beam-pointing drifts, the two-sample deviation scales as $1/\sqrt{n}$. We indeed observe a scaling exponent of $-0.48(1)$, which demonstrates the long-term stability of the ion beam over the entire period of about 9 h. The minimal two-sample deviation of the beam position yields a long-term beam-pointing stability of 1.5 nm [Fig. 1(b)].

Imaging with single ions.—We demonstrate imaging of transmissive structures by scanning a photonic waveguide-cavity fabricated from diamond (see Fig. 2). We received this sample (300 nm thickness, fabricated with Ga^+ ion FIB) from the group of C. Becher [22].

For the acquisition of the image in Fig. 2(b), each pixel is probed with one ion. Gating the detector by the extraction event (gate time typically less than 200 ns) ensures that the dark count rate (< 100 s^{-1}) does not affect the image contrast. The contrast in transmissive areas is assumed to be limited solely by the detector efficiency, resulting in binomial counting statistics. The detector efficiency was measured to be $96 \pm 2\%$. Other influences such as background gas collisions are considered to be negligible. For comparison with a conventional approach, Fig. 2(c) shows the same structure but imaged with an experimentally emulated Poissonian source: Prior to probing each pixel, the number of ions to be extracted is obtained using a random number generator with a Poisson-distributed output, where the mean value is set to 1. The SNR for the deterministic source is 4.90 compared with 0.96 for the emulated Poissonian source. This is calculated by assuming a detector efficiency of 0.96, negligible dark counts, and SNR $= \mu/\sigma$,

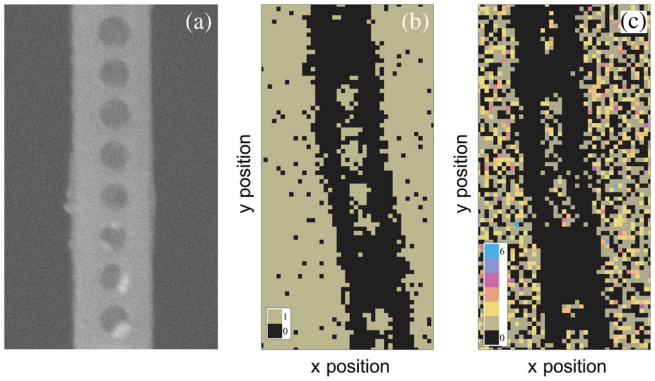

FIG. 2. (a) SEM image of the waveguide-cavity structure. Holes have a diameter of about 150 nm. (b) Scan of the cavity structure using one ion at each lateral position, with a resolution of (25×25) nm^2 per pixel. The entire information in the picture is based on 2659 transmission events out of 4141 extracted ions. (c) Imaging a source with emulated Poissonian behavior: The lower SNR as compared to (c) is clearly visible. Missing holes compared to (a) are attributed to blind holes. Here, image information is based on 2420 transmission events out of 3694 extracted ions.

where μ is the mean value, and σ is the standard deviation of the corresponding probability mass function.

Compared with a Poissonian source with flux Φ_{Pois}, a deterministic source requires a flux of only $\Phi_{\mathrm{det}} = \Phi_{\mathrm{Pois}}(1-a)$ to achieve the same SNR, where a is the efficiency of the detector. For our deterministic microscope, the same SNR as a corresponding Poissonian microscope can be achieved with only 4% of the flux.

Bayes experimental design.—We maximize the spatial information gain per probe event by harnessing the Bayesian experimental design method [23–26]. Employing this technique, one can measure parameters of structures that can be modeled by a parametrized transmission function determined from some prior knowledge of the geometry. We first introduce the method by means of the profiling edge measurement and demonstrate how the radius and position of the beam can be obtained more efficiently as compared to the stepwise profiling method. In a second example, an algorithm is presented which is able to find and determine the lateral position of a circular hole structure with optimal efficiency.

In the Bayesian approach to parameter estimation, the knowledge about the value of a parameter θ given by preexisting information is expressed by the *prior* probability distribution function (PDF) $p(\theta)$. Information from the outcome y of a new measurement is subsequently incorporated using the Bayes update rule yielding a *posterior* PDF:

$$p(\theta|y,\xi) = \frac{p(y|\theta,\xi)p(\theta)}{p(y|\xi)}. \tag{1}$$

Here, the right-hand side is the product of the prior PDF and the statistical model of the measurement $p(y|\theta,\xi)$, which is the probability of observing an outcome y given the parameter values θ and design parameters ξ. ξ contains the free control parameters of the experiment. Normalization is provided by the marginal probability of observing y, $p(y|\xi) = \int p(y|\theta,\xi)p(\theta)d\theta$.

Use of Bayesian experimental design maximizes the information gain per measurement by an appropriate choice of the design parameters. The information gain of a measurement with outcome y and control parameters ξ is expressed by the *utility* $U(y,\xi)$, which is the difference in the Shannon entropies of the posterior and prior PDFs:

$$U(y,\xi) = \int \ln[p(\theta|y,\xi)]p(\theta|y,\xi)d\theta - \int \ln[p(\theta)]p(\theta)d\theta.$$

Averaging the utility over the measurement outcomes yields a quantity independent of the hitherto unknown observation:

$$U(\xi) = \sum_{y\in\{0,1\}} U(y,\xi)p(y|\xi), \tag{2}$$

which can be optimized with respect to ξ. Carrying out the measurement with control parameters ξ, in this way, ensures optimal information gain.

For the profiling edge measurement, the design parameter is the profiling edge position, while the parameters to be determined are beam position x_0, 1σ radius, and detector efficiency a, i.e., $\theta = (x_0, \sigma, a)$. The outcome of the measurement is binary, $y = \{0,1\}$. The measurement is modeled as

$$p(y|\theta,\xi) = \begin{cases} \frac{a}{2}\mathrm{erfc}\left[\frac{\xi - x_0}{\sigma\sqrt{2}}\right] & \text{if } y = 1, \\ 1 - \frac{a}{2}\mathrm{erfc}\left[\frac{\xi - x_0}{\sigma\sqrt{2}}\right] & \text{if } y = 0, \end{cases}$$

which, in this case, is a convolution of the transmission function of the structure to be imaged and a Gaussian beam profile.

The experimental sequence is carried out as follows. The initial prior, a three-dimensional joint PDF, for the parameters x_0, σ, and a is chosen. Its marginals can be uniform or an educated guess, e.g., a Gaussian distribution. It is implemented numerically, being a three-dimensional grid of equidistant, weighted, and normalized sampling points. For updating the prior to enable the utility calculation (2), the Bayes update (1) is performed for each sampling point. The maximizing algorithm is realized by calculating the utility for an interval divided into equidistant profiling edge positions and recursively repeating this calculation for a smaller interval around the maximum. Five recursions were found to be sufficient to reach the required accuracy without incurring excessive computational expense. Here, integrals are replaced by sums over all sampling points. Using the measurement outcome of the real experiment performed at the calculated optimal profiling edge position, the Bayesian update (1) is applied to calculate the posterior PDF, which assumes the role of the prior PDF for the next iteration. The procedure is repeated until an accuracy goal is reached.

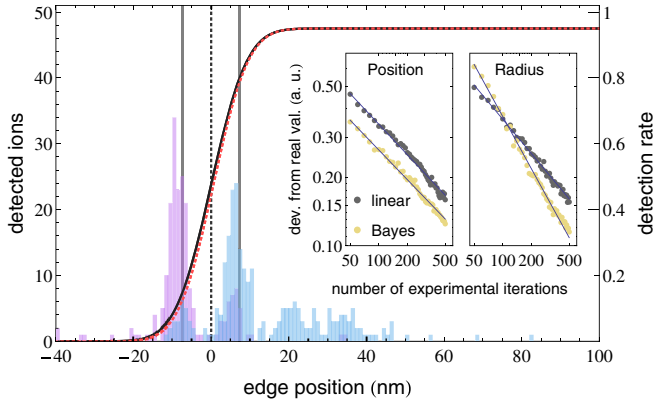

FIG. 3. Histogram of optimal blade positions. These data from 500 events are split into cases where the ion was detected (blue) and cases where it was not (purple). Bayes fit function $p(y = 1|\theta, \xi)$ is shown according to the final parameter values (black), radius $\sigma = 7.18 \pm 0.89$ nm, and detector efficiency $a = 0.95 \pm 0.02$. The zero of the x axis is set to x_0. For comparison, the result of a maximum likelihood fit (dashed red) to the entire data, with $\sigma = 7.13 \pm 0.66$ nm and $a = 0.95 \pm 0.02$, $x_0 = 0.73$ nm. The inset shows the average deviation of the simulation results from the real value as a function of the number of iterations, using 1000 independent simulation runs for each data point. A multiplicative speed-up of a factor of $\approx 4/3$ is found in determining the beam position and an exponential speed-up from $n^{-0.5}$ to $n^{-0.76}$ in determining the radius when using the Bayesian method.

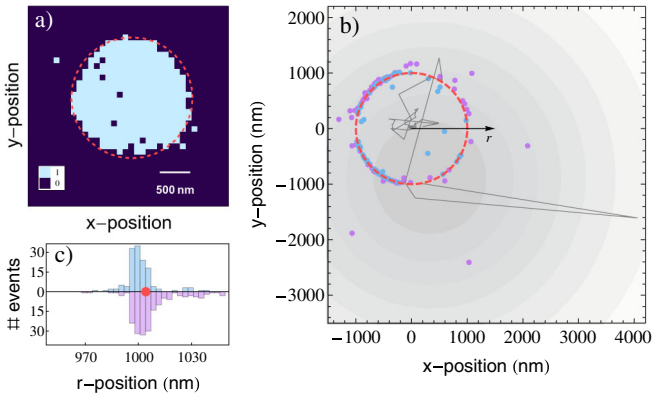

FIG. 4. (a) A circular hole structure is scanned using one ion at each lateral position, with a resolution of 100×100 nm^2 per pixel. The red circle shows the result of a maximum likelihood fit to the data. (b) The same structure is measured using the Bayes experimental design method. For the plot, the x and y positions of the hole were set to zero. The blue and red dots represent the positions where an ion was, or was not, detected, respectively. The final location and radius of the hole structure is depicted by the dashed circle. The initial guess of the Gaussian-shaped PDF for the position is depicted as a gray shade in the background. The dark gray line follows the progression of its mean value, i.e., the assumed center position of this distribution as a function of the number of extracted ions. Within the first four iterations, no ion is transmitted. The spatial information of these blocked particles shifts the assumed position, since it excludes that specific areas are transmissive. After the first ion is transmitted, the assumed position makes a step towards its location. (c) shows a histogram of detected and not detected events dependent on r the distance to the center of the structure.

Figure 3 shows the result of a typical Bayes-optimized profiling edge measurement. The parameter values for the Bayes fit function are derived by calculating the mean values of the marginal PDFs of the corresponding parameters. For comparison, a maximum likelihood fit is also shown, since values determined by the Bayesian method are, in principle, not independent of the exact sequence. To compare the stepwise method with the Bayesian method, we implement numerical simulations of both approaches and calculate the average deviation of the simulation outcome from the real value as a function of the number of iterations n (inset Fig. 3).

We demonstrate the measurement of parameter values of two-dimensional transmissive structures with a parametrizable transmission function by means of a circular hole in a diamond sample (see Fig. 4). This is also a practical example for sample alignment, since for many applications, such as the deposition of dopants, it is useful to know the exact lateral position of a sample with respect to the beam focus. For comparison, the hole structure is first scanned with a linear sequence using 1332 ions in total, where each lateral position is probed with one ion. A maximum likelihood fit to the data yields a precision of $\Delta x = 47.1$ nm and $\Delta y = 22.6$ nm for the position, where the radius was extracted to be $r = 1057 \pm 32$ nm.

For applying the Bayesian method, the experiment is parametrized by the lateral position of the center of the circular hole, its radius, as well as the 1σ beam radius and the detector efficiency. The radius of the beam and detector efficiency were kept constant at 25 nm and 95% respectively. Both values were measured separately in advance. Using 379 ions in total, the position was determined with a precision of $\Delta x = 2.7$ nm and $\Delta y = 2.1$ nm, where the radius was measured to be $r = 1004 \pm 2$ nm. Systematic errors resulting from the deviations of the shape to the parametrization (ideal circle) are difficult to quantify, since the precise extent of this deviation is unknown. However, the precision of the results apply to an ideal circular shape, which could be available in other experiments. Although this means a strict comparison in terms of precision per probe event is not possible, it can be concluded that the average information gain per probe event provided by the Bayes method is significantly higher due to more targeted probing.

Future prospects.—In future experiments, the microscope may be improved by increasing the repetition rate to ≈ 125 s^{-1} through remote loading from a magneto-optical trap [27]. This could be further improved by generating a constantly refilled reservoir of cold trapped ions, from where single ions are shuttled to an extraction site. Using a multisegmented planar trap could enable one to operate many such reservoirs in parallel. Reliability and also resolution could be improved by integrating the source into a commercial ion beam column featuring high mechanical

stability. The temporal control of the ions down to the picosecond regime may also enable ultrafast time resolved microscopy and stroboscopic measurements. Moreover, the time-of-flight information could be used to switch the focusing fields and, in this way, circumvent the resolution-limiting Scherzer theorem [28], which states that a rotationally symmetric ion optical lens with static electromagnetic fields excluding space charges always exhibits unavoidable spherical and chromatic aberrations. Through optical pumping, it is feasible to implement a fully spin-polarized source, e.g., for sensing magnetic polarization of surfaces as pioneered in electron microscopy [29]. Ultimately, the combination of control of internal and external degrees of freedom of the ion could allow for the realization of matter wave interferometry with single ions [30,31].

The apparatus was also conceived for deterministic ion implantation on the nanometer scale. This would enable fabrication of scalable solid-state quantum devices such as systems of coupled nitrogen vacancy color centers [32], coupled single phosphorous nuclear spins in silicon [33–36], and cerium or praseodymium in yttrium orthosilicate [37]. Here, imaging and implantation are highly complementary, since absolute referencing via imaging of the sample is essential for accurate positioning of dopants.

The authors acknowledge discussions with S. Prawer and G. Schönhense. The team acknowledges financial support by the Volkswagen-Stiftung (atomic nanoassembler), the DFG-Forschergruppe (FOR 1493), and the EU projects DIAMANT and SIQS (both FP7-ICT). F. S. K. thanks the DFG for financial support in the DIP program (FO 703/2-1).

*georg.jacob@uni-mainz.de
†Present address: National Laboratory for Physical Sciences at Microscale and Department of Modern Physics, University of Science and Technology of China, Shanghai 201315, People's Republic of China.

[1] M. Knoll and E. Ruska, Das Elektronenmikroskop, Z. Phys. **78**, 318 (1932).
[2] E. W. Müller, Versuche zur Theorie der Elektronenemission unter der Einwirkung hoher Feldstärken, Phys. Z. **37**, 838 (1936).
[3] E. W. Müller and K. Bahadur, Field ionization of gases at a metal surface and the resolution of the field ion microscope, Phys. Rev. **102**, 624 (1956).
[4] W. H. Escovitz, T. R. Fox, and R. Levi-Setti, Scanning transmission ion microscope with a field ion source, Proc. Natl. Acad. Sci. U.S.A. **72**, 1826 (1975).
[5] J. Orloff and L. Swanson, Study of a field-ionization source for microprobe applications, J. Vac. Sci. Technol. **12**, 1209 (1975).
[6] B. Ward, J. A. Notte, and N. Economou, Helium ion microscope: A new tool for nanoscale microscopy and metrology, J. Vac. Sci. Technol. B **24**, 2871 (2006).
[7] R. Erni, M. D. Rossell, C. Kisielowski, and U. Dahmen, Atomic-Resolution Imaging with a Sub-50-pm Electron Probe, Phys. Rev. Lett. **102**, 096101 (2009).
[8] D. Kruger, P. Schneck, and H. Gelderblom, Helmut Ruska and the visualisation of viruses, Lancet **355**, 1713 (2000).
[9] N. Bassim, K. Scott, and L. A. Giannuzzi, Recent advances in focused ion beam technology and applications, MRS Bull. **39**, 317 (2014).
[10] B. Knuffman, A. Steele, and J. McClelland, Cold atomic beam ion source for focused ion beam applications, J. Appl. Phys. **114**, 044303 (2013).
[11] P. Hommelhoff, C. Kealhofer, A. Aghajani-Talesh, Y. R. Sortais, S. M. Foreman, and M. A. Kasevich, Extreme localization of electrons in space and time, Ultramicroscopy **109**, 423 (2009).
[12] A. McCulloch, D. Sheludko, S. Saliba, S. Bell, M. Junker, K. Nugent, and R. Scholten, Arbitrarily shaped high-coherence electron bunches from cold atoms, Nat. Phys. **7**, 785 (2011).
[13] P. Hommelhoff, C. Kealhofer, and M. A. Kasevich, Ultrafast Electron Pulses from a Tungsten Tip Triggered by Low-Power Femtosecond Laser Pulses, Phys. Rev. Lett. **97**, 247402 (2006).
[14] A. G. Manning, R. Khakimov, R. G. Dall, and A. G. Truscott, Single-Atom Source in the Picokelvin Regime, Phys. Rev. Lett. **113**, 130403 (2014).
[15] C. Ates, I. Lesanovsky, C. S. Adams, and K. J. Weatherill, Fast and Quasideterministic Single Ion Source from a Dipole-Blockaded Atomic Ensemble, Phys. Rev. Lett. **110**, 213003 (2013).
[16] W. Schnitzler, N. M. Linke, R. Fickler, J. Meijer, F. Schmidt-Kaler, and K. Singer, Deterministic Ultracold Ion Source Targeting the Heisenberg Limit, Phys. Rev. Lett. **102**, 070501 (2009).
[17] K. Izawa, K. Ito, H. Higaki, and H. Okamoto, Controlled extraction of ultracold ions from a linear paul trap for nanobeam production, J. Phys. Soc. Jpn. **79**, 124502 (2010).
[18] Y.-M. Kim, H. Y. Jeong, S.-H. Hong, S.-Y. Chung, J. Y. Lee, and Y.-J. Kim, Practical approaches to mitigation of specimen charging in high-resolution transmission electron microscopy, J. Vac. Sci. Technol. B **1**, 134 (2010).
[19] S. Prawer and R. Kalish, Ion-beam-induced transformation of diamond, Phys. Rev. B **51**, 15711 (1995).
[20] K. Singer, U. G. Poschinger, M. Murphy, P. A. Ivanov, F. Ziesel, T. Calarco, and F. Schmidt-Kaler, Colloquium: Trapped ions as quantum bits: Essential numerical tools, Rev. Mod. Phys. **82**, 2609 (2010).
[21] J. C. Meyer, C. O. Girit, M. Crommie, and A. Zettl, Imaging and dynamics of light atoms and molecules on graphene, Nature (London) **454**, 319 (2008).
[22] J. Riedrich-Möller, L. Kipfstuhl, C. Hepp, E. Neu, C. Pauly, F. Mücklich, A. Baur, M. Wandt, S. Wolff, M. Fischer *et al.*, One- and two-dimensional photonic crystal microcavities in single crystal diamond, Nat. Nanotechnol. **7**, 69 (2012).
[23] D. V. Lindley, On a measure of the information provided by an experiment, Ann. Math. Stat. **27**, 986 (1956).
[24] C. Guerlin, J. Bernu, S. Deleglise, C. Sayrin, S. Gleyzes, S. Kuhr, M. Brune, J.-M. Raimond, and S. Haroche, Progressive field-state collapse and quantum non-demolition photon counting, Nature (London) **448**, 889 (2007).
[25] L. Pezzé, A. Smerzi, G. Khoury, J. F. Hodelin, and D. Bouwmeester, Phase Detection at the Quantum Limit with Multiphoton Mach-Zehnder Interferometry, Phys. Rev. Lett. **99**, 223602 (2007).

[26] S. Brakhane, W. Alt, T. Kampschulte, M. Martinez-Dorantes, R. Reimann, S. Yoon, A. Widera, and D. Meschede, Bayesian Feedback Control of a Two-Atom Spin-State in an Atom-Cavity System, Phys. Rev. Lett. **109**, 173601 (2012).

[27] J. M. Sage, A. J. Kerman, and J. Chiaverini, Loading of a surface-electrode ion trap from a remote, precooled source, Phys. Rev. A **86**, 013417 (2012).

[28] G. Schönhense and H. Spiecker, Correction of chromatic and spherical aberration in electron microscopy utilizing the time structure of pulsed excitation sources, J. Vac. Sci. Technol. B **20**, 2526 (2002).

[29] T. Duden and E. Bauer, Spin-polarized low energy electron microscopy, Surf. Rev. Lett. **05**, 1213 (1998).

[30] M. Arndt, A. Ekers, W. von Klitzing, and H. Ulbricht, Focus on modern frontiers of matter wave optics and interferometry, New J. Phys. **14**, 125006 (2012).

[31] F. Hasselbach, Progress in electron- and ion-interferometry, Rep. Prog. Phys. **73**, 016101 (2010).

[32] F. Dolde, I. Jakobi, B. Naydenov, N. Zhao, S. Pezzagna, C. Trautmann, J. Meijer, P. Neumann, F. Jelezko, and J. Wrachtrup, Room-temperature entanglement between single defect spins in diamond, Nat. Phys. **9**, 139 (2013).

[33] B. E. Kane, A silicon-based nuclear spin quantum computer, Nature (London) **393**, 133 (1998).

[34] D. N. Jamieson, C. Yang, T. Hopf, S. Hearne, C. Pakes, S. Prawer, M. Mitic, E. Gauja, S. Andresen, F. Hudson *et al.*, Controlled shallow single-ion implantation in silicon using an active substrate for sub-20-keV ions, Appl. Phys. Lett. **86**, 202101 (2005).

[35] J. J. Pla, K. Y. Tan, J. P. Dehollain, W. H. Lim, J. J. Morton, F. A. Zwanenburg, D. N. Jamieson, A. S. Dzurak, and A. Morello, High-fidelity readout and control of a nuclear spin qubit in silicon, Nature (London) **496**, 334 (2013).

[36] M. Veldhorst, C. Yang, J. Hwang, W. Huang, J. Dehollain, J. Muhonen, S. Simmons, A. Laucht, F. Hudson, K. Itoh, A. Morello, and A. Dzurak, A two-qubit logic gate in silicon, Nature (London) **526**, 410 (2015).

[37] R. Kolesov, K. Xia, R. Reuter, R. Stöhr, A. Zappe, J. Meijer, P. Hemmer, and J. Wrachtrup, Optical detection of a single rare-earth ion in a crystal, Nat. Commun. **3**, 1029 (2012).